

Full length article

A comprehensive analytical model for laser powder-fed additive manufacturing



Yuze Huang, Mir Behrad Khamesee, Ehsan Toyserkani (PhD PEng)*

University of Waterloo, Department of Mechanical and Mechatronics Engineering, Waterloo, Ontario N2L 3G1, Canada

ARTICLE INFO

Article history:

Received 13 February 2016

Received in revised form 28 April 2016

Accepted 8 July 2016

Available online 30 July 2016

Keywords:

Laser powder-fed additive manufacturing

Additive manufacturing

Analytical model

Powder spatial distribution

Directed energy deposition

ABSTRACT

This paper addresses a comprehensive analytical model for the laser powder-fed additive manufacturing (LPF-AM) process, also known as directed energy deposition AM. The model analytically couples the moving laser beam with Gaussian energy distribution, the powder stream and the semi-infinite substrate together, while considering the attenuated laser power intensity distribution, the heated powder spatial distribution and the melt pool 3D shape with its boundary variation. The particles concentration on transverse plane is modeled with Gaussian distribution based on optical measurement. The model can effectively be used for process development/optimization and controller design, while predicting adequate clad geometry as well as the catchment efficiency rapidly. Experimental validation through the deposition of Inconel 625 proves the model can accurately predict the clad geometry and catchment efficiency in the range of specific energy that is corresponding to high clad quality (maximum percentage difference is 6.2% for clad width, 7.8% for clad height and 6.8% for catchment efficiency).

© 2016 Elsevier B.V. All rights reserved.

1. Introduction

The laser powder-fed additive manufacturing (LPF-AM) process is one of the seven classes of AM that falls under the “Directed Energy Deposition” class. The functionality of LPF-AM has attracted multiple industries to embrace its features for coating, repair and part production from single or multiple materials. In the LPF-AM process, the powder stream interacts with the laser beam and attenuates the beam intensity, while the heated powder particles impinge into the melt pool adding mass and energy to the melt pool to form effective deposition. All these interactions affect the melt pool temperature distribution and the final shape of the clad layer.

A comprehensive model is essential to provide the process fluctuation prediction required for the design of comprehensive controllers for real-time closed-loop control of the process [1]. For the development of any closed-loop control algorithm for LPF-AM, the addition of a model-based benchmark is required. However, the model must be fast, simple but accurate enough to stabilize the controller. Therefore, finite elements models are not suitable for this purpose [2]. Analytical model that can effectively be incorpo-

rated in high speed hardware may provide a great platform for the real-time control of LPF-AM.

Numerical methods based on finite element methods have also proved popular and can accurately simulate the powder flux distribution [3], laser particle interaction process [4], melt pool formation [5], clad layer geometry [6,7], temperature, velocity and thermal stress fields distribution over the process [8,9]. But such numerical models are increasing the complexity of process modeling and computational time.

Analytical modeling is a classic way for understanding the unfamiliar aspects of the process [10] and acts as a benchmark reference generator inside the structure of closed-loop control system. Picasso et al. [11] established a simple but realistic analytical model for LPF-AM. The powder attenuation effect for the laser beam was accounted with simple geometry intersecting ratio. The heated powder energy was added together with the laser beam energy as the heat source to calculate the substrate temperature field. With the relative simplicity, their model can produce immediate results about scanning speed, powder feed rate and catchment efficiency. Fathi et al. [12] developed a mathematical model of LPF-AM to predict the melt pool depth, dilution and the temperature field with given values of clad height and clad width. They built the mathematical top surface of the melt pool with parabolic equation and solved the heat conduction in substrate to predict the temperature field based on an infinite moving point heat source. Tan et al. [13] built an analytical model to estimate the clad layer geomet-

* Corresponding author at: Department of Mechanical and Mechatronics Engineering, University of Waterloo, Waterloo, Ontario N2L 3G1, Canada.
E-mail address: ehsan.toyserkani@uwaterloo.ca (E. Toyserkani).

Nomenclature

A_{S_2}, A_{S_3}	Melt pool effective projection area, mm ²
C	Specific heat capacity, J/(kg K)
D	Laser spot diameter, mm
E	Specific energy, J/mm ²
\dot{g}	Argon gas feed rate, dL/min
h	Clad height, mm
H	Nozzle height, mm
$I(x,y,z)$	Laser beam intensity at point (x, y, z) , W
$I_A(x,y,z)$	Attenuated laser beam intensity at point (x, y, z) , W
$I_p(x,y,z)$	Heated powder energy intensity, W
$I_{net}(x,y,z)$	Resultant energy source intensity
k	Thermal conductivity, W/(m K)
K	Constant for powder stream boundary line
L	Melt pool length, mm
l_1, l_2	Major semi-axis of the projection ellipse
L_f	Latent heat fusion, J/Kg
m_p	Particle mass, g
\dot{m}	Powder feed rate, g/min
$n(x',y',z')$	Powder number concentration
P_L	Laser power, W
Q_{ext}	Extinct coefficient
r_0	Nozzle internal radius, mm
r_p	Particle radius, μm
$r(z'), r(z)$	Powder stream effective radius at z', z mm
R_{0L}	Laser beam waist radius, mm
$R_L(z)$	Laser beam effective radius at z , mm
S_1, S_2, S_3	Melt pool approximation inclined surface
t_n	Nozzle tube thickness (mm)
T_0	Ambient temperature, K
T_m	Material melting temperature, K
$T_p(x, y, z)$	Particle temperature at point (x, y, z) , K
v	Process speed, m/s
v_p	Particle velocity, m/s
w	Minor semi-axis of the projection ellipse, mm
W	Melt pool width, mm
z_0	Laser beam waist position, mm
ΔT	Temperature increment, K
ϕ	Melt pool inclination angle, <i>degree</i>
α	Thermal diffusivity, m ² /s
α_w	Brewster effect coefficient
β	Powder laser absorptivity
β_w	Substrate laser power absorptivity
η	Catchment efficiency
θ	Powder stream divergence angle, <i>degree</i>
θ_L	Laser beam far-field divergence angle, <i>rad</i>
λ_L	Fiber laser wavelength, μm
μ	Thermal conductivity correction factor
$\rho(x',y',z')$	Powder spatial mass concentration, g/mm ³
ρ_p	Particle density, Kg/m ³
σ	Extinction cross section of a sphere particle, mm ²
φ	Nozzle angle, <i>degree</i>
Ω	Melt pool boundary

try based on a moving disc heat source model. The melt pool was fitted as an ellipse and the powder catchment efficiency was calculated directly as melt pool and the powder stream area ratio. They also considered the powder flux distribution in clad height prediction and pointed out that both the melt pool length and clad width increasing with decreasing scanning velocity and increasing laser power. Shengfeng et al. [14] proposed a similar analytical model to predict the cladding height and catchment efficiency with assuming the melt pool to be a flat plane on substrate. Experi-

mental results show that the catchment efficiency has the same varying trend with the nozzle angle. Xinyong et al. [15] developed a mathematical model to estimate the catchment efficiency based on mass conservation and kinematic equations, but no consideration was paid to the interaction effect between the laser beam and the particles.

Most of the above analytical models have decoupled the mass and energy flows, ignored the changes of the laser power absorptivity due to the varying of clad geometry (Brewster effect), and calculated the melt pool limits only based upon laser power source. As a result, those models may have different prediction accuracy. Based on these papers, we built a comprehensive analytical model for LPF-AM. The novelty of the model is based on the fact that it unifies the main physical changes of the whole process by coupling the attenuated laser power, the heated powder stream and the semi-infinite substrate with considering their concentration and intensity spatial distribution. In addition, the catchment efficiency model takes into account both the powder spatial distribution and the melt pool shape variation.

2. Analytical modelling

An analytical model for laser powder-fed additive manufacturing has been developed in this paper with the following assumptions:

- (1) The lateral nozzle has a perfect circular outlet.
- (2) The gas–powder flow is assumed as a steady state flow and the effect of the gravity and drag force are considered negligible. Thus, the powder stream has a uniform velocity in transverse direction which is assumed to be the same as the gas velocity near the nozzle outlet.
- (3) The convection and radiation losses in the powder stream was not considered and the particles are isothermal with spherical geometry [16].
- (4) Powder particles, impinging onto the molten pool, are considered effectively added to and mixed with the liquid flow on melt pool surface. It is required that the adhesion force F_{ad} is bigger than and the repelling force F_r ($F_{ad}/F_r > 1$) between the melt pool surface and the impinging particle. Lin [17] calculated the ratio of $F_{ad}/F_r = 100$ for stainless steel in coaxial LPF-AM, which testifies that the powder is effectively melted and attached onto the molten pool surface. The liquid phases will then rapidly mixed and become homogeneous due to the strong convection currents generated by the thermal gradients on melt pool surface (Marangoni convection/effect) [18,19].
- (5) The thermo-physical properties for both powder and substrate are considered to be temperature independent. Average values over the temperature variation were considered in the model.

2.1. Powder spatial distribution

The schematic of LPF-AM is shown in Fig. 1. The laser beam scans in the positive y -direction with the process velocity v , and the origin of its coordinates is fixed at the center of the laser beam spot on the substrate. The nozzle has an inclined angle φ and distance H with respect to the substrate plane. The laser beam and the powder stream interact with each other after point P .

The powder concentration mode in the transverse direction was identified with Gaussian distribution by Lin [20] with both optical techniques and the theory of particles diffusion and convection in gaseous medium based on Fuchs's aerosols laminar flow. Optical luminance experimental analysis of Pinkerton's research [21] verified that the particles stream have Gaussian concentration profiles in the transverse plane. Yang [22] and Gangxian [23] also built the

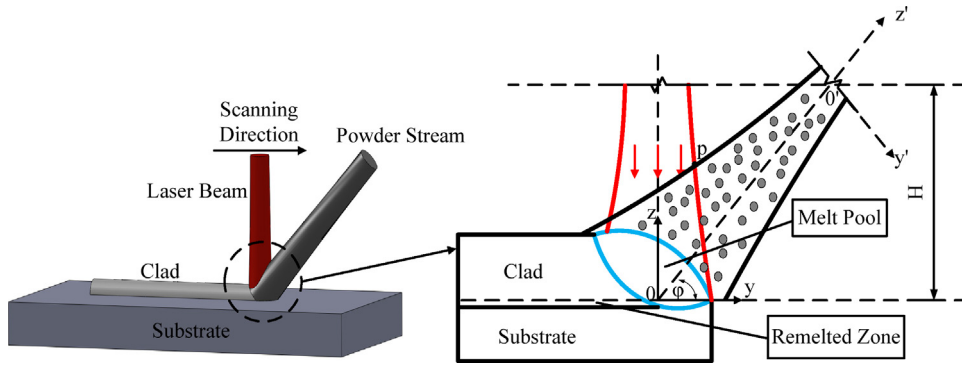


Fig. 1. Schematic diagram for laser powder-fed additive manufacturing.

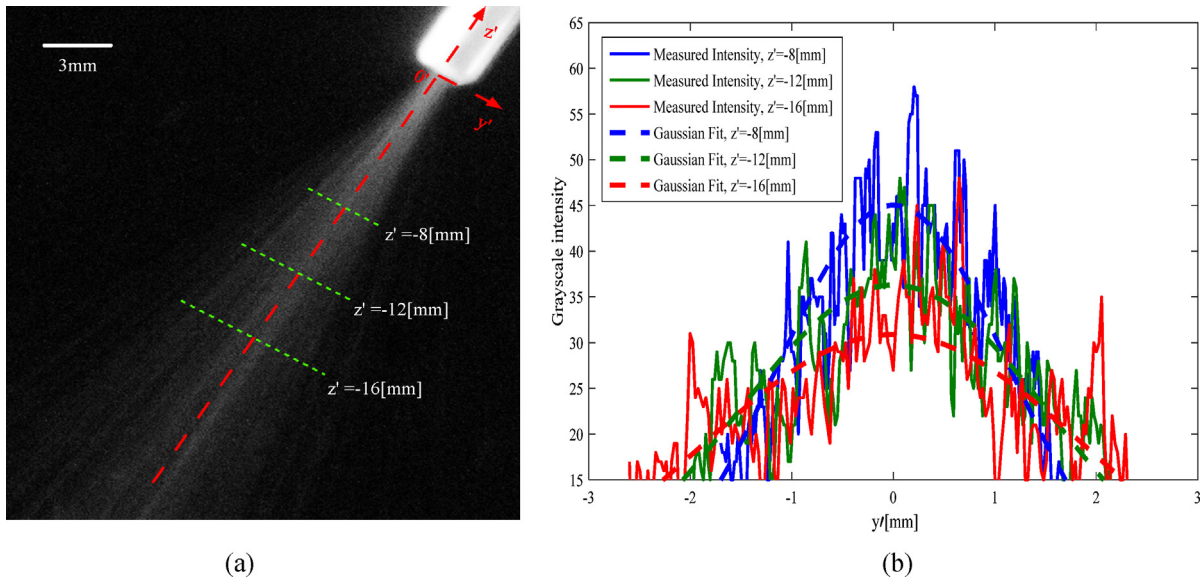


Fig. 2. Inconel 625 powder stream grayscale intensity distribution measurement ($\dot{m} = 5(\text{g}/\text{min})$, $\phi = 60^\circ$, $\dot{g} = 2.5(\text{dL}/\text{min})$, $r_0 = 0.7(\text{mm})$): (a) Grayscale image with transversal green dot lines (b) Measured grayscale intensity distribution with Gaussian fitting results on transversal lines.

powder stream concentration with a Gaussian model and the model predicted values were consistent with the experimental results. In this paper, the powder concentration distributions in the transverse plane were expressed by the powder stream luminance distributions. Based on Mie theory, the luminance of the powder stream is proportional to particles concentration, so the luminance distribution in the image expresses the particles concentration distribution within the powder stream. The powder stream images were taken by a Canon EOS 60D camera (Canon, Oita, Japan) with a Pentacon 135 mm f/2.8 lens (Pentacon, Dresden, Germany). The powder stream luminance was measured by grayscale intensity with MATLAB Image-Processing Software, in which the RGB images were converted to grayscale images. As the Inconel 625 powder stream grayscale image shown in Fig. 2, the powder concentration has Gaussian distribution in transverse plane with varying distances.

From the results, powder spatial mass concentration $\rho(x', y', z')$ and the number concentration $n(x', y', z')$ can be derived as

$$\rho(x', y', z') = \frac{2\dot{m}}{v_p \pi r^2(z')} \exp \left[-\frac{2(x'^2 + y'^2)}{r^2(z')} \right] \quad (1)$$

$$n(x', y', z') = \frac{2\dot{m}}{v_p m_p \pi r^2(z')} \exp \left[-\frac{2(x'^2 + y'^2)}{r^2(z')} \right] \quad (2)$$

where \dot{m} is the powder feed rate, m_p the average mass for each particle, $v_p = \dot{g}/\pi r_0^2$ the average powder velocity (based on assump-

tion 2), \dot{g} the gas flow rate, r_0 the nozzle internal radius and $r(z')$ is the effective radius of powder stream reaching $1/e^2$ of the peak concentration value of the powder stream center [23]. Based on the measurement and derivation highlighted in Appendix A, the effective radius of powder stream can be expressed as

$$r(z') = r_0 - z' \tan \theta, \quad z' < 0 \quad (3)$$

where θ is the effective divergence angle. Considering the coordinates transformation from $x'y'z'$ to xyz

$$x' = x$$

$$y' = (y - H/\tan \phi) \sin \phi - (z - H) \cos \phi \quad (4)$$

$$z' = (y - H/\tan \phi) \cos \phi + (z - H) \sin \phi$$

Then the powder mass concentration in xyz coordinates will be derived as

$$\rho(x, y, z) = \frac{2\dot{m}}{v_p \pi r^2(z)} \exp \left[-\frac{2 \left[x^2 + [(y - H/\tan \phi) \sin \phi - (z - H) \cos \phi]^2 \right]}{r^2(z)} \right], \quad (5)$$

$$r(z) = - \left[(y - H/\tan \phi) \cos \phi + (z - H) \sin \phi \right] \tan \theta + r_0$$

2.2. Laser beam and gas-powder stream interaction

The laser beam and consequently its power intensity is attenuated by the powder stream during their interaction [16,18]. The

total attenuation is a sum effect of scattering and absorption, which is also named as extinction.

This paper uses a Gaussian TEM₀₀ mode laser power with intensity distribution as [19]

$$I(x, y, z) = \frac{2P_L}{\pi R_L^2(z)} \exp \left[-\frac{2(x^2 + y^2)}{R_L^2(z)} \right] \quad (6)$$

where P_L is the laser power, $R_L(z)$ is the effective radius of the laser beam at a distance $\Delta z = z_0 - z$ from the beam waist position z_0 with R_{0L} radius for the laser beam and far-field divergence angle θ_L . $R_L(z)$ is expressed as [19]

$$R_L(z) = \sqrt{R_{0L}^2 + 4\theta_L^2(z_0 - z)^2} \quad (7)$$

The laser power intensity that is attenuated by powder stream with dz distance could be calculated based on Mie' theory [18,24]

$$dI = -\sigma I(x, y, z)n(x, y, z)dz \quad (8)$$

where $I(x, y, z)$ is the laser intensity at point (x, y, z) , σ the extinction cross section of a sphere particle ($\sigma = Q_{ext}\pi r_p^2$), Q_{ext} the extinct coefficient, and r_p is the mean radius of the particles. $n(x, y, z)$ can be calculated by

$$n(x, y, z) = \frac{2im}{v_p m_p \pi r^2(z)} \exp \left[-\frac{2 \left[x^2 + \left[(y - H/\tan\varphi)\sin\varphi - (z - H)\cos\varphi \right]^2 \right]}{r^2(z)} \right] \quad (9)$$

In LPF-AM process, as the particle size is much bigger than the laser wavelength, it is reasonable to assume that the extinction coefficient $Q_{ext} = 1$ [18,25] and most of the attenuated laser energy is absorbed by the particle. Eq. (8) is derived from the first-order approximation of the Mie's theory, which calculates the total attenuation or extinction power for the laser beam travels through the powder stream and is valid when $2\pi r_p/\lambda_L < 300$ [18]. In this study, the average particle radius $r_p = 42$ (μm), laser wavelength $\lambda_L = 1.06$ (μm), therefore the condition is satisfied. We should point out that this criterion is only considered when the scattering is included for total attenuated power calculation. But in the LPF-AM process, r_p is normally much larger than λ_L , the powder absorption is the predominant attenuation type. Thus, Eq. (8) can be directly used based on Lambert-Beer law without considering this condition [8,20,21].

where β is the powder laser absorptivity, c_p the material specific heat capacity, and ρ_p is the average particle density. Integrating Eq. (12) over the interaction length in z -axis allows the particle temperature $T_p(x, y, z)$ to be calculated as

$$T_p(x, y, z) = T_0 + \frac{3\beta}{4 \sin\varphi v_p c_p \rho_p r_p} \int_z^{\bar{z}_p(y)} I_A(x, y, z) dz \quad (13)$$

where $\bar{z}_p(y) = z_p(-y)$ is the symmetrical line of $z_p(y)$ about z -axis, and T_0 is the ambient temperature. The path of integration from z to $\bar{z}_p(y)$ was used to approximate the particle traveling distance component in the laser beam transverse direction.

As the powder impinges onto the melt pool, it draws energy to increase its enthalpy to that of the melt pool in a short time [25]. Thus, the heated powder energy intensity $I_p(x, y, z)$ is expressed as a negative energy source. It should be noted that the heated powder does add positive energy to the melt pool, therefore the negative energy source defining here is used to couple the powder mass flow with the melt pool under the consideration of melt pool energy variation due to the added powder.

$$I_p(x, y, z) = c_p \rho(x, y, z) [T_p(x, y, z) - T_m] \quad (14)$$

2.3. Thermal conduction on substrate

On the substrate surface, the coming energy from the attenuated laser beam $I_A(x, y, z)$ and heated powder flux $I_p(x, y, z)$ are summed up and treated as a bulk heating source. Thus, the resultant energy source intensity $I_{net}(x, y, z)$

$$I_{net}(x, y, z) = I_A(x, y, z) + I_p(x, y, z) \quad (15)$$

For a moving heat source on a semi-infinite work-piece surface, the temperature field $T(x, y, z)$ could be expressed based on Rosenthal's equation [26]

$$T(x, y, z) - T_0 = \frac{P_L}{2\pi k} \frac{e^{-v(x+R)/2\alpha}}{R}, \quad R = \sqrt{x^2 + y^2 + z^2}, \quad (16)$$

where P_L is the laser beam power, k the thermal conductivity, α the thermal diffusivity, and v is the process velocity. With considering the resultant energy intensity distribution, the temperature field on substrate is derived by integrating Eq. (16) over the laser beam area based on superposition.

where β_w is the substrate laser power absorptivity. In order to approach reality more precise platform, the latent heat of fusion, thermo-capillary phenomena (Marangoni effect) and the varying laser power absorptivity (Brewster effect) are taking into consideration with the following approximations.

- The effect of latent heat fusion L_f on temperature distribution can be approximated by increasing the specific heat capacity c^* as [27]

$$c_p^* = \frac{L_f}{T_m - T_0} + c_p \quad (18)$$

- The effect of Marangoni flow can be accounted by using the modified thermal conductivity k^* with a correction factor μ as [7]

$$k^*(T) = \mu k(T_m), \quad T > T_m \quad (19)$$

- The absorption of an inclined plane for a linearly polarized laser beam is affected by the plane inclination angle (Brewster effect)

$$T(x, y, z) - T_0 = \frac{1}{2\pi k} \int_{\xi=-r_L(z)}^{\xi=r_L(z)} \int_{\eta=-\sqrt{r_L^2(z)-\xi^2}}^{\eta=\sqrt{r_L^2(z)-\xi^2}} \left[\beta_w I_A(\xi, \eta, z) + c_p \rho(\xi, \eta, z) (T_p(\xi, \eta, z) - T_m) \right] \times \frac{\exp \left[-v(y - \eta + R)/2\alpha \right]}{R} d\eta d\xi, \quad R = \sqrt{(x - \xi)^2 + (y - \eta)^2 + z^2} \quad (17)$$

As shown in Fig. 1, the powder stream and laser beam will be interacted with each other after point P . The attenuated laser beam intensity $I_A(x, y, z)$ may be calculated with the integration of Eq. (8) over the interaction length in z -axis as

$$I_A(x, y, z) = I(x, y, z) \exp \left[-\sigma \int_z^{z_p(x,y)} n(x, y, z) dz \right] \quad (10)$$

where $z_p(x, y)$ is the upper surface of the powder stream, which is approximated with the powder stream top boundary line $z_p(y)$

$$z_p(y) = K + (y - K/\tan\varphi) \cdot \tan(\varphi - \theta), \quad (K = H + r_0 \sin\varphi/\tan\theta, \quad \varphi > 0) \quad (11)$$

The powder absorbs energy from the laser beam during their interaction, and the absorbed energy increases the particles temperature. Based on assumption 3, the temperature increment ΔT for time interval $\Delta t = dz/v_p \sin\varphi$ follows the energy balance equation

$$\beta I_A(x, y, z) \pi r_p^2 \Delta t = c_p \rho_p \frac{4}{3} \pi r_p^3 \Delta T \quad (12)$$

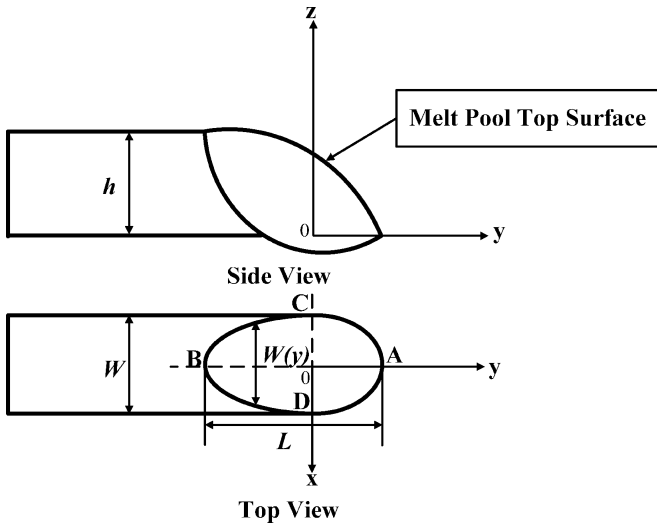


Fig. 3. Schematic diagram for melt pool geometry.

[11]. For our case, the laser beam is circularly polarized and the absorptivity $\beta_w(\phi)$ can be expressed as [6,26]

$$\beta_w(\phi) = \beta_w(0)(1 + \alpha_w\phi) \quad (20)$$

where ϕ is the inclination angle, $\beta_w(0)$ the laser power absorptivity for a flat plane, and α_w is a constant coefficient depends on the material. For the sake of simplification, the inclination angle is approximated based on the clad height h and laser beam diameter D

$$\phi = \tan^{-1}\left(\frac{h}{D}\right) \quad (21)$$

2.4. Melt pool geometry

Melt pool projection limits on substrate surface is approximated by the solid-liquid line. Eq. (17) is simplified as

$$T(x, y, z) - T_0 = \Gamma(x, y, z) \quad (22)$$

As shown in Fig. 3, points A, B, C and D are located on the boundary of the melt pool, according to Eq. (22), the coordinate values can be calculated as

$$\begin{cases} \Gamma(y_A, 0, 0) = T_m - T_0, y_A > 0 \\ \Gamma(y_B, 0, 0) = T_m - T_0, y_B < 0 \\ \Gamma(0, x_D, 0) = T_m - T_0, x_D > 0 \\ \Gamma(0, x_C, 0) = T_m - T_0, x_C < 0 \end{cases} \quad (23)$$

The projection of the melt pool on substrate plane has the boundary Ω

$$\Omega = \{y_B \leq y \leq y_A, x_C \leq x \leq x_D\}, \quad L = y_A - y_B, W = |x_C| = |x_D| \quad (24)$$

where L and W are the melt pool length and width for boundary Ω , respectively. The boundary of the melt pool is approximated by two half ellipses with same minor semi-axis of $W/2$ (The left part has a major semi-axis of $|y_B|$ and the right part has major semi-axis of $|y_A|$). With considering the melt pool top surface boundary as a parabolic curve, the melt pool top surface is expressed as [12]

$$z(x, y) = \left[-h \frac{(y - y_B)^2}{(y_A - y_B)^2} + h\right] \cdot \left(1 - \frac{4x^2}{W^2(y)}\right), (x \in [x_C, x_D], y \in [y_B, y_A]) \quad (25)$$

The width of the melt pool $W(y)$ can be expressed as

$$W(y) = \begin{cases} W \cdot \sqrt{\left(1 - \frac{y^2}{y_A^2}\right)}, y \geq 0 \\ W \cdot \sqrt{\left(1 - \frac{y^2}{y_B^2}\right)}, y < 0 \end{cases} \quad (26)$$

2.5. Clad geometry

With dividing the substrate surface into small elemental patches dS , each patch is so small that the powder flow density over it is essentially uniform. The powder mass dm that impinged onto dS in an elemental elapsed time can be approximated as

$$dm = \rho(x, y, 0) \cdot dS \cdot v_p \sin \varphi \quad (27)$$

The clad height on dS area can be calculated based on the sum of the powder impinging onto it during the dwelling time

$$h_{dS} = \frac{1}{\rho_p dS} \int_0^{D/v} dm dt \quad (28)$$

Then, for any point within the melt pool boundary, the clad height can be derived as

$$h(x, y) = \lim_{\delta \rightarrow 0} h_{dS} = \frac{2 \sin \varphi D \dot{m}}{v \rho_p \pi r^2(z=0)} \exp\left[-\frac{2[x^2 + [(y - H/\tan \varphi) \sin \varphi + H \cos \varphi]^2]}{r^2(z=0)}\right], \\ (x, y) \in \Omega \quad (29)$$

where δ is the largest diameter of patch dS . Based on Eq. (29), the original clad height h_0 is estimated with an average value over the laser beam spot boundary and the process clad height h (along the laser scanning direction) is calculated over the melt pool boundary Ω . The clad width is approximated with the melt pool width $W(y)$ as expressed by Eq. (26).

2.6. Catchment efficiency

The melt pool has a curved top surface as derived in Section 2.4, which has an inclined angle with the substrate surface. Particles that fall into the melt pool surface are considered to be effectively integrated with melt pool based on assumption 4. To calculate the melt pool effective area in the coming powder stream, the melt pool is approximated by an inclined surface S_1 , which is then projected to powder transverse planes S_2 and S_3 that cuts through the highest and lowest point of the melt pool top surface, respectively (see Appendix B). The particles number probability density for per unit time per unit area on powder stream transverse plane can be expressed as

$$f(x', y', z') = \frac{n(x', y', z)}{\int_{-\infty}^{+\infty} \int_{-\infty}^{+\infty} n(x', y', z) dx' dy'} = \frac{2}{\pi r_p^2(z')} \exp\left[-\frac{2(x'^2 + y'^2)}{r_p^2(z')}\right] \quad (30)$$

Then the catchment efficiency can be derived as the integration of the particle number probability over the melt pool projection area on the powder transverse plane. By integrating Eq. (30) over the effective projection area A_{S_2} and A_{S_3} , the overall catchment efficiency is derived as

$$\eta = \frac{\int_{A_{S_2}} f(x', y', z') dx' dy' + \int_{A_{S_3}} f(x', y', z') dx' dy'}{2} \quad (31)$$

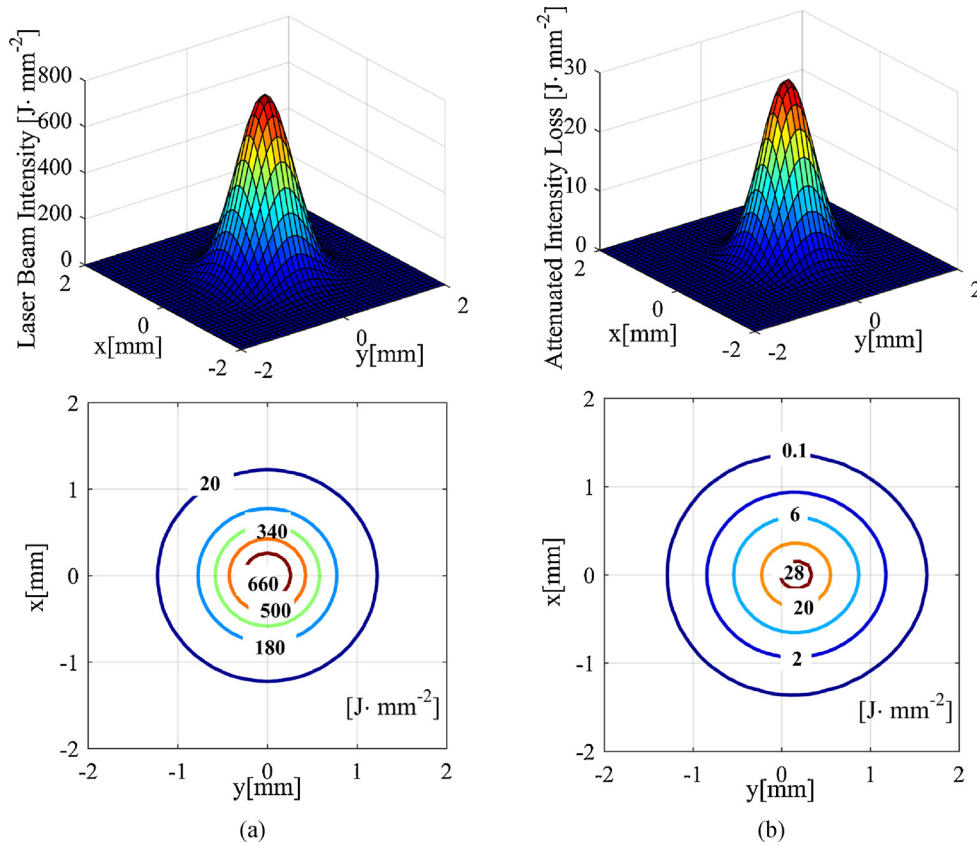


Fig. 4. Laser beam intensity distribution on the substrate surface (a) Without attenuation (b) Attenuated laser intensity loss by Inconel 625 powder ($\dot{m} = 7(g/min)$, $P_L = 1000(W)$, $r_0 = 0.7(mm)$, $\dot{g} = 2.5(dL/min)$).

3. Numerical analysis

The attenuated laser beam intensity distribution and the temperature contour on substrate surface were simulated in this part by MATLAB software with parameters listed in Section 4.

The laser beam is attenuated by the powder stream before it reaches the substrate. The model simulation results for Inconel 625 powder stream attenuation is shown in Fig. 4(b), the largest attenuated laser intensity loss is around 28 $[J/mm^2]$. Fig. 4(a) shows the original laser beam intensity distribution on substrate with maximum intensity 660 $[J/mm^2]$. Compared to the largest attenuation intensity loss with the original maximum laser intensity, a maximum laser beam attenuation percentage can be predicted around 4%.

With coupling the attenuated laser beam and the heated powder stream as the resultant moving heat source, the temperature field on substrate surface is shown in Fig. 5. Melt pool projection geometry on the substrate surface is approximated with two half ellipses (the dash line shown in Fig. 5), which fits well with the calculated melt pool temperature 1563(k) that identifying the solid-liquid interface.

4. Materials and fabrication procedure

Inconel 625 powder (Carpenter, Bridgeville, Pennsylvania, USA). Ni60.82%, Cr 21.4%, Mo 8.76%, Nb 3.31%, Fe 4.72%, Si 0.58% and Mn 0.41%, wt% with particle size 45–125 μm (Gaussian distribution) was deposited on Inconel 625 plates (McMaster-Carr, Aurora, Ohio, USA) by a LPF-AM setup developed in-house. This setup includes a continuous IPG photonics fiber laser with the maximum power of 1100W installed in a Fadal CNC machine. The powder feeder purchased from Sulzer Metco was used to feed materials

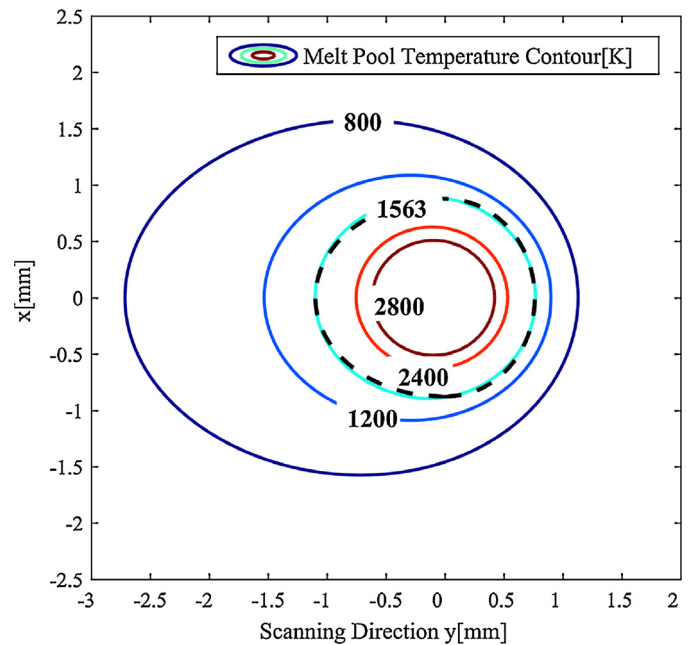


Fig. 5. Melt pool temperature distribution on Inconel 625 substrate surface ($\dot{m} = 5(g/min)$, $v = 7.5(mm/s)$, $P_L = 1000(W)$, $r_0 = 0.7(mm)$, $\dot{g} = 2.5(dL/min)$).

through a lateral nozzle. The Inconel 625 plates had the dimensions of $75 \times 15 \times 5(mm^3)$. For both the clad and the substrate, the thermo-physical properties of Inconel 625 are considered to be temperature independent, and the thermal parameters are calculated based on the mean values over the temperature range as

Table 1
Inconel 625 thermo-physical properties [28].

Density ρ_p [Kg/m ³]	Thermal conductivity k [W m ⁻¹ K ⁻¹]	Specific heat capacity C [J kg ⁻¹ K ⁻¹]	Melting temperature T_m [K]
8440	9.8(21 °C)–25.6 (1000 °C)	410(21 °C)–670 (1090 °C)	1563(1290 °C)

Table 2
Laser metal direct deposition process parameters.

Parameters	Values	Parameters	Values
Process velocity (v)	3, 4.5, 6, 7.5 (mm/s)	Laser power (P_L)	1000(W)
Powder feed rate (\dot{m})	5, 7 (g/ min)	Absorptivity (β)	35%[29]
Fiber laser wavelength(λ_L)	1.06 (μm)	Latent heat of fusion (L_f)	204500(J/Kg)[29]
Beam waist radius (R_{0L})	0.43(mm)	Far-field divergence angle (θ_L)	0.02 (rad)
Beam waist position(z_0)	19.8 (mm)	Argon gas feed rate (\dot{g})	2.5 (dL/ min)
Nozzle height (H)	7(mm)	Nozzle angle (ϕ)	60°
Nozzle internal radius (r_0)	0.7 (mm)	Laser spot diameter (D)	1.8 (mm)
Nozzle tube thickness (t_n)	0.8 (mm)	Brewster effect coefficient (α_w)	0.0196
Correction factor (μ)	2.5		

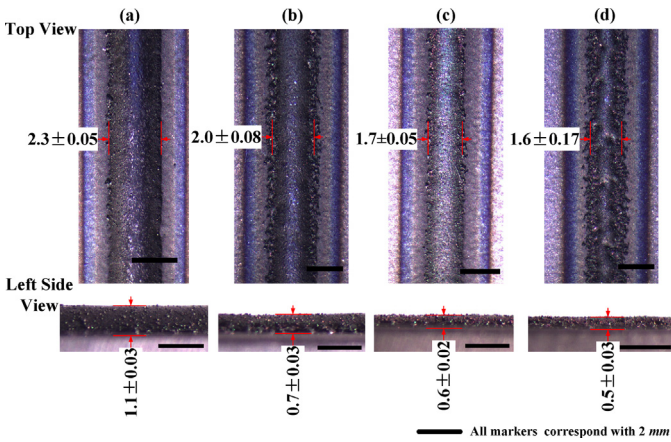


Fig. 6. Inconel 625 single layer deposition profile by LPF-AM, $\dot{m} = 7(\text{g}/\text{min})$ (a) $E = 185.2(\text{J} \cdot \text{mm}^{-2})$, (b) $E = 123.5(\text{J} \cdot \text{mm}^{-2})$, (c) $E = 92.6(\text{J} \cdot \text{mm}^{-2})$ (d) $E = 74.1(\text{J} \cdot \text{mm}^{-2})$.

listed in Table 1. Single layer deposition experiments were done to test the model with varying process velocity and powder feed rate. Each group experiment was repeated five times and the process parameters are listed in Table 2.

To measure the LPF-AM powder catchment, the attached powder was evaluated by weighing the substrate before and after deposition, the total ejected powder was calculated with the product of the powder feed rate and deposition time. Then the experimental catchment efficiency was evaluated as the ratio of that attached powder weight divided by ejected powder weight. The clad width and clad height were measured by optical microscopy.

5. Results and discussion

During the clad formation in LPF-AM, the input energy from the laser beam is used to heat the moving substrate and the incoming powder, which is mainly influenced by laser power, process velocity and powder feed rate. In this paper, a combined parameter specific energy $E = P_L/vD$ [19], which describes the energy delivered by the laser power per unit feed rate area of the laser track, was used to address the process and validate the analytical model with comparing the modeled and measured clad dimension and catchment efficiency.

Fig. 6 shows the single layer deposition profiles of Inconel 625 at different specific energy. As seen, the layer profiles keep smooth

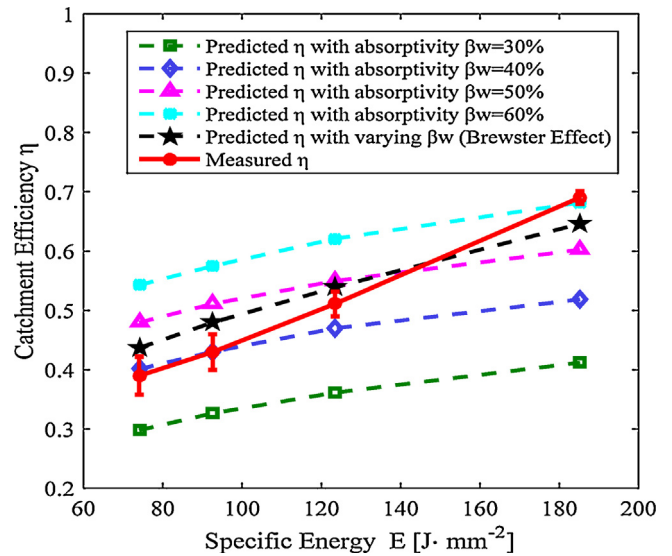


Fig. 7. Model predicted and measured catchment efficiency ($\dot{m} = 5(\text{g}/\text{min})$).

with a higher specific energy ((a) (b) and (c)). And both the clad width and height increase with the increasing of specific energy.

Fig. 7 shows that the built model successfully predicts the experimentally observed trend of that catchment efficiency increasing with increasing specific energy. But it also shows that there will be great gaps between the predicted and the measured catchment value if the laser power absorptivity is set to a stable value (30%, 40%, 50% or 60%). On the contrary, as the Brewster effect describes, the results match well by using varying laser power absorptivity. In this paper, an average Brewster effect coefficient α_w was calculated by adjusting the laser power absorptivity $\beta_w(\phi)$ to match the measured catchment efficiency based on Eqs. (20)–(21).

Fig. 8 compares the modeled and measured clad widths, clad heights and catchment efficiencies with varying specific energy and powder feed rate. The experimental results have low standard deviation values, indicating an excellent repeatability and precision. The model matches well with the experimental results. With increasing specific energy, the clad width, melt pool length, clad height and catchment efficiency increase as well, which is consistent with the results in references [13,14]. For a given condition in the LPF-AM process, the higher specific energy means there is more laser power at per unit area of laser track, which enlarges the melt pool area as well as the powder catchment.

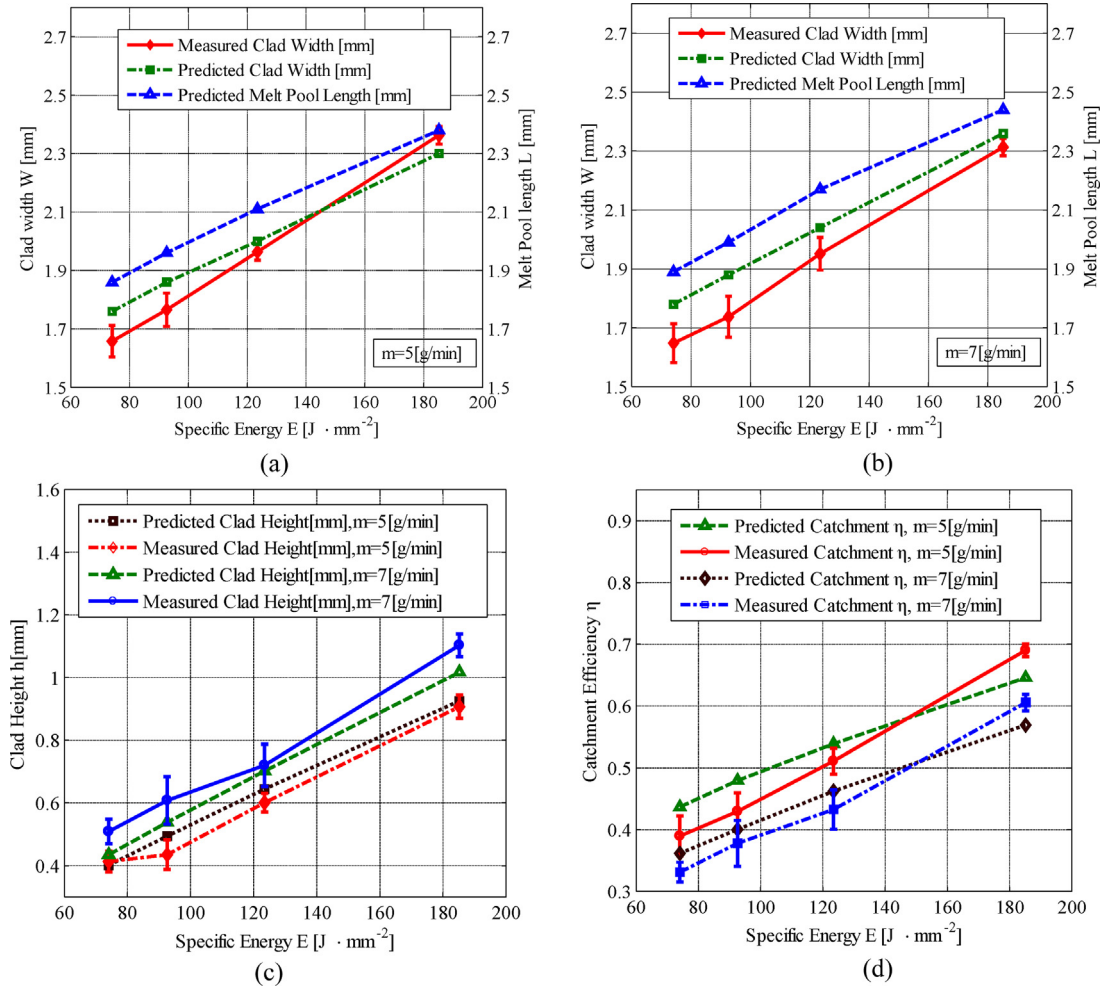


Fig. 8. Experimental and model predicted results comparison, (a), (b) and (c) clad geometry, (d) catchment efficiency.

From Fig. 8(a), (c) and (d), it can be seen that for a given powder feed rate ($\dot{m} = 5$ (g/min)) the predicted clad width, clad height and catchment efficiency are bigger than the measured results but with increasing the specific energy, the difference gap is smaller or disappear, which may be attributed to an elevated radiative and convective heat losses. This causes the melt pool not to have enough energy to melt the total incoming powder at lower specific energy. But for higher specific energy, the measured results are bigger than the predicted results. The higher specific energy increases the powder catchment as well as the clad height and its non-planar geometrical features. With an elevated clad height at a relatively fixed width, the wetting angle increases thus the laser power absorptivity is increased due to Brewster effect. The model uses an average Brewster effect coefficient to compensate the increasing absorptivity, which is smaller than the real time-varying laser power absorptivity. This may be one of the reasons for the disagreement of the measured and predicted clad height shown in Fig. 8 (c) for a higher powder feed rate ($\dot{m} = 7$ (g/min)).

There are other sources of discrepancies between the modelling and experimental results. Major source of errors may attribute to the simplification assumptions listed in Section 2. In particular, considering the thermal/optical parameters based on the mean values over the temperature range may highly contribute to the discrepancies. The assumptions to ignore gravity, drag force, convection, and radiation losses, and consider effective particle attachment to the melt pool, provide a reasonable solution to couple the mass

flux (powder stream), the heat flux (laser beam) and the melt pool with analytical functions. The temperature independent thermal parameter calculation simplifies the model and provides closed form solutions for the powder stream and melt pool temperature analytical integrations.

In the range 100–190 (J/mm^{-2}) for the specific energy, the maximum percentage difference for the model predicted and experimental results are 6.2% for the clad width, 7.8% for the clad height and 6.8% for the catchment efficiency. These results validate the accuracy of the model.

The developed model has the potential to effectively be used for designing comprehensive controllers for the process by incorporating into high speed hardware platform. And the model can be expanded to multi-nozzle LPF-AM setups [e.g., LENS technology from Optomec] by combining each single powder stream as shown in references [16,25]. The modified procedure for adding multiple nozzles to the analytical model is listed as follows:

1. Build the effective radius r_i for each single powder stream with the optical method in Appendix A, leading to new equations of $\rho_i(x, y, z)$, $n_i(x, y, z)$, $I_{A_i}(x, y, z)$ and $I_{p_i}(x, y, z)$ for each nozzle based on Eqs. (1)–(14).
2. For the powder stream above the consolidation plane, the combined powder flux ($\rho(x, y, z)$, $n(x, y, z)$, $I_p(x, y, z)$) and laser flux $I_A(x, y, z)$ can be developed with integrating each nozzle flux (from step 1) based on superposition principle.

3. New resultant energy source intensity $I_{net}(x, y, z)$ can be built with Eq. (15).
4. For the powder stream beyond the consolidation plane, it has two options depending on the powder stream distribution [16]. (1) For lower powder velocity nozzle, experiments in references [21,30] have testified that the powder stream is Gaussian distribution. New effective radius and nozzle flux can be built with repeating steps 1–3. (2) For high powder velocity nozzle, the powder stream beyond the consolidation plane will keep discrete and divergent, it is recommended to continue the integration model above the consolidation plane and rebuild the $I_p(x, y, z), I_A(x, y, z)$ and $I_{net}(x, y, z)$ based on Eqs. (10)–(15).
5. Build the melt pool 3D geometry, clad geometry and process catchment efficiency model based on Eqs. (17)–(31) with incorporating the results from steps 1–3.

6. Conclusion

An analytical model of LPF-AM was developed in this paper. The attenuated laser power and heated powder stream flow were coupled together with Gaussian intensity distribution. By substituting the coupled energy into the Rosenthal’s 3D moving heat source model, and combining with the calculated clad height, the 3D melt pool geometry was built with consideration of the Brewster effect. A solution to calculate the process catchment efficiency was developed with considering the powder concentration distribution, the melt pool inclination and boundary variation. Experimental validation using Inconel 625 shows the model can accurately predict the clad geometry as well as the process catchment efficiency in the case of high clad quality expected. The built analytical model can provide a proper platform for the design of controllers for LPF-AM using high speed hardware.

Acknowledgements

The authors would like to acknowledge the financial support of the Natural Sciences and Engineering Research Council of Canada (NSERC) and China Scholarship Council (CSC).

Appendix A. Powder stream effective radius

The effective radius of powder stream is defined as one that reduced to $1/e^2$ of the peak concentration value in the stream center. As the luminance distribution in the CCD camera image expresses the particles concentration in the powder stream based on Mie theory, so the effective radius can be measured by the luminance value of the CCD camera image that reduced to $1/e^2$ of the center luminance value. The grey values of the images for the powder stream in transverse direction were measured by ImageJ

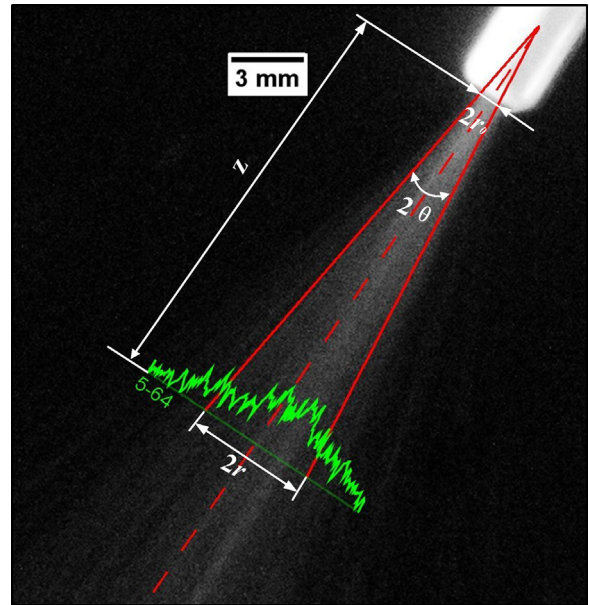


Fig. A1. Powder stream effective divergence angle measurement.

software, which shows a Gaussian distribution (Fig. A1). Then the effective radius of powder stream $r(z)$ at a distance z with the nozzle outlet can be measured in ImageJ. For simplification of the modeling, the powder stream is approximated with circular cone geometry. And the effective radius of powder stream can be derived as

$$r(z) = r_0 + z \tan \theta \tag{A.1}$$

In which θ is the effective divergence angle, r_0 is the nozzle internal radius. Cold flow experiments were designed to measure the effective divergence angle with various settings of nozzle internal diameter, argon gas velocity and powder feed rate by a CCD camera (see Table A1).

Appendix B. Effective melt pool projection area

To calculate the effective melt pool projection area, the melt pool top surface is approximated by the inclined surface S_1 that cuts through its highest point E and lowest point A . Then S_1 is projected to powder transverse planes S_2 and S_3 with the effective projection area A_{S_2} and A_{S_3} as shown in Fig. B1.

Based on the 3D melt pool geometry function built in Section 2.4 (Eqs. (25)–(26)), the melt pool projections on inclined surfaces S_2 and S_3 are approximated with the geometry of ellipses.

Table A1
Powder stream effective divergence angles.

Powder feed rate (g/min)	Argon gas feed rate (dL/min)	$r_0 = 0.35(mm)$		$r_0 = 0.7(mm)$		$r_0 = 0.8(mm)$	
		Divergence Angle (°)	Valid for (mm)	Divergence Angle (°)	Valid for (mm)	Divergence Angle (°)	Valid for (mm)
3	2.5	4.5 ± 0.2	Z < 18	5.8 ± 0.2	Z < 20	6.4 ± 0.2	Z < 24
3	3.5	4.7 ± 0.2	i < 18	6 ± 0.2	Z < 20	6.8 ± 0.2	Z < 24
3	4.5	5.2 ± 0.2	Z < 17	6.4 ± 0.2	Z < 19	7.1 ± 0.2	Z < 23
5	2.5	5.7 ± 0.2	Z < 17	6.8 ± 0.2	Z < 18	7.6 ± 0.2	i < 24
5	3.5	6.4 ± 0.2	Z < 17	8 ± 0.2	Z < 18	8.1 ± 0.2	Z < 22
5	4.5	6.6 ± 0.2	Z < 17	8.4 ± 0.2	i < 18	8.5 ± 0.2	Z < 22
7	2.5	7.3 ± 0.2	Z < 16	8.6 ± 0.2	Z < 17	9 ± 0.2	Z < 21
7	3.5	7.7 ± 0.2	Z < 16	8.9 ± 0.2	Z < 17	9.5 ± 0.2	Z < 20
7	4.5	8.1 ± 0.2	Z < 16	9.3 ± 0.2	Z < 17	9.8 ± 0.2	Z < 20

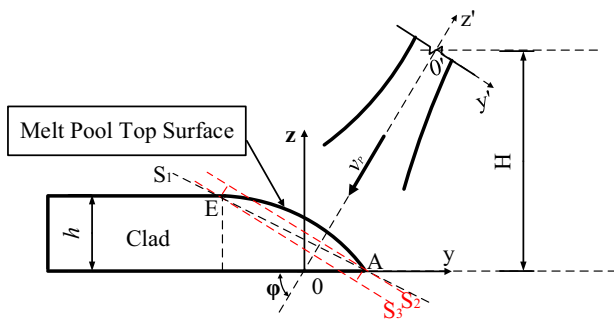


Fig. B1. Melt pool projection on powder transverse plane.

Projection area A_{S_2} :

$$\begin{cases} \frac{y'^2}{l_1^2} + \frac{x'^2}{w^2} = 1, z' = z_{S_2}, y' \in [-l_1, 0], x' \in \left[-\frac{w}{2}, \frac{w}{2}\right] \\ \frac{y'^2}{l_2^2} + \frac{x'^2}{w^2} = 1, z' = z_{S_2}, y' \in [0, l_2], x' \in \left[-\frac{w}{2}, \frac{w}{2}\right] \end{cases} \quad (\text{B.1})$$

Projection area A_{S_3} :

$$\begin{cases} \frac{y'^2}{l_1^2} + \frac{x'^2}{w^2} = 1, z' = z_{S_3}, y' \in [-l_1, 0], x' \in \left[-\frac{w}{2}, \frac{w}{2}\right] \\ \frac{y'^2}{l_2^2} + \frac{x'^2}{w^2} = 1, z' = z_{S_3}, y' \in [0, l_2], x' \in \left[-\frac{w}{2}, \frac{w}{2}\right] \end{cases} \quad (\text{B.2})$$

where l_1 and l_2 is the major semi-axis of the ellipse projection area A_{S_2} and A_{S_3} , respectively, and can be calculated based on geometric relationships as shown in Fig. B1. w is the minor semi-axis, which is parallel with the substrate surface and is equal to half of the melt pool projection width on substrate surface.

References

- [1] A. Fathi, A. Khajepour, E. Toyserkani, M. Durali, Clad height control in laser solid freeform fabrication using a feedforward PID controller, *Int. J. Adv. Manuf. Technol.* 35 (2006) 280–292, <http://dx.doi.org/10.1007/s00170-006-0721-1>.
- [2] E. Toyserkani, A. Khajepour, S. Corbin, Application of experimental-based modeling to laser cladding, *J. Laser Appl.* 14 (2002) 165, <http://dx.doi.org/10.2351/1.1494079>.
- [3] I. Taberner, A. Lamikiz, E. Ukar, L.N. López de Lacalle, C. Angulo, G. Urbikain, Numerical simulation and experimental validation of powder flux distribution in coaxial laser cladding, *J. Mater. Process. Technol.* 210 (2010) 2125–2134, <http://dx.doi.org/10.1016/j.jmatprotec.2010.07.036>.
- [4] S.Y. Wen, Y.C. Shin, J.Y. Murthy, P.E. Sojka, Modeling of coaxial powder flow for the laser direct deposition process, *Int. J. Heat Mass Transf.* 52 (2009) 5867–5877, <http://dx.doi.org/10.1016/j.ijheatmasstransfer.2009.07.018>.
- [5] Y. Lee, M. Nordin, S. Babu, D. Farson, Influence of fluid convection on weld pool formation in laser cladding, *Weld. J.* 93 (2014) 2925–3005.
- [6] E. Toyserkani, A. Khajepour, S. Corbin, Three-dimensional finite element modeling of laser cladding by powder injection: effects of powder feedrate and travel speed on the process, *J. Laser Appl.* 15 (2003) 153, <http://dx.doi.org/10.2351/1.1585087>.
- [7] E. Toyserkani, A. Khajepour, S. Corbin, 3-D Finite element modeling of laser cladding by powder injection: effects of laser pulse shaping on the process, *Opt. Lasers Eng.* 41 (2004) 849–867, [http://dx.doi.org/10.1016/S0143-8166\(03\)00063-0](http://dx.doi.org/10.1016/S0143-8166(03)00063-0).
- [8] X. He, J. Mazumder, Transport phenomena during direct metal deposition, *J. Appl. Phys.* 101 (2007) 053113, <http://dx.doi.org/10.1063/1.2710780>.
- [9] M. Alimardani, E. Toyserkani, J.P. Huissoon, A 3D dynamic numerical approach for temperature and thermal stress distributions in multilayer laser solid freeform fabrication process, *Opt. Lasers Eng.* 45 (2007) 1115–1130, <http://dx.doi.org/10.1016/j.optlaseng.2007.06.010>.
- [10] A.J. Pinkerton, Advances in the modeling of laser direct metal deposition, *J. Laser Appl.* 27 (2015) S15001, <http://dx.doi.org/10.2351/1.4815992>.
- [11] M. Picasso, C.F. Marsden, J.-D. Wagnière, A. Frenk, M. Rappaz, A simple but realistic model for laser cladding, *Metall. Mater. Trans. A* 25 (1994) 281–291, <http://dx.doi.org/10.1007/BF02665211>.
- [12] A. Fathi, E. Toyserkani, A. Khajepour, M. Durali, Prediction of melt pool depth and dilution in laser powder deposition, *J. Phys. D: Appl. Phys.* 39 (2006) 2613–2623, <http://dx.doi.org/10.1088/0022-3727/39/12/022>.
- [13] H. Tan, J. Chen, F. Zhang, X. Lin, W. Huang, Estimation of laser solid forming process based on temperature measurement, *Opt. Laser Technol.* 42 (2010) 47–54, <http://dx.doi.org/10.1016/j.optlastec.2009.04.016>.
- [14] S. Zhou, X. Dai, H. Zheng, Analytical modeling and experimental investigation of laser induction hybrid rapid cladding for Ni-based WC composite coatings, *Opt. Laser Technol.* 43 (2011) 613–621, <http://dx.doi.org/10.1016/j.optlastec.2010.09.001>.
- [15] X. Gong, Y. Zhang, M. Liu, Powder transport model for laser cladding by lateral powder feeding: I. Powder flow field with cylindrical distribution, *Int. J. Adv. Manuf. Technol.* 67 (2012) 2501–2509, <http://dx.doi.org/10.1007/s00170-012-4667-1>.
- [16] A.J. Pinkerton, An analytical model of beam attenuation and powder heating during coaxial laser direct metal deposition, *J. Phys. D: Appl. Phys.* 40 (2007) 7323–7334, <http://dx.doi.org/10.1088/0022-3727/40/23/012>.
- [17] J. Lin, A simple model of powder catchment in coaxial laser cladding, *Opt. Laser Technol.* 31 (1999) 233–238, [http://dx.doi.org/10.1016/S0030-3992\(99\)00046-8](http://dx.doi.org/10.1016/S0030-3992(99)00046-8).
- [18] A. Frenk, M. Vandyoussefi, J. Wagniere, Analysis of the laser-cladding process for stellite on steel, *Mater. Trans. B* (1997), <http://dx.doi.org/10.1007/s11663-997-0117-0>.
- [19] E. Toyserkani, A. Khajepour, S. Corbin, *Laser cladding*, CRC Press, 2004.
- [20] J. Lin, Concentration mode of the powder stream in coaxial laser cladding, *Opt. Laser Technol.* 31 (1999) 251–257, [http://dx.doi.org/10.1016/S0030-3992\(99\)00049-3](http://dx.doi.org/10.1016/S0030-3992(99)00049-3).
- [21] A.J. Pinkerton, L. Li, Modelling powder concentration distribution from a coaxial deposition nozzle for laser-based rapid tooling, *J. Manuf. Sci. Eng.* 126 (2004) 33, <http://dx.doi.org/10.1115/1.1643748>.
- [22] N. Yang, Concentration model based on movement model of powder flow in coaxial laser cladding, *Opt. Laser Technol.* 41 (2009) 94–98, <http://dx.doi.org/10.1016/j.optlastec.2008.03.008>.
- [23] G. Zhu, D. Li, A. Zhang, G. Pi, Y. Tang, The influence of laser and powder defocusing characteristics on the surface quality in laser direct metal deposition, *Opt. Laser Technol.* 44 (2012) 349–356, <http://dx.doi.org/10.1016/j.optlastec.2011.07.013>.
- [24] C. Bohren, D. Huffman, Absorption and scattering of light by small particles (2008) <http://dx.doi.org/10.1002/9783527618156>.
- [25] A.J. Pinkerton, R. Moat, K. Shah, L. Li, M. Preuss, P.J. Withers, A verified model of laser direct metal deposition using an analytical enthalpy balance method, <http://eprints.lancs.ac.uk/59694/>, 2007 (accessed 28.04.16).
- [26] W. Steen, J. Mazumder, *Laser material processing*, Springer Science & Business Media, 2010.
- [27] S. Brown, H. Song, Finite element simulation of welding of large structures, *J. Eng. Ind.* 114 (1992) 441, <http://dx.doi.org/10.1115/1.2900696>.
- [28] Special Metals, Inconel alloy 625, accessed 7.02.16, <http://www.specialmetals.com/assets/documents/alloys/inconel/inconel-alloy-625.pdf>.
- [29] N. Ahmed, K.T. Voisey, D.G. McCartney, Investigation into the effect of beam shape on melt pool characteristics using analytical modelling, *Opt. Lasers Eng.* 48 (2010) 548–554, <http://dx.doi.org/10.1016/j.optlaseng.2009.12.013>.
- [30] J. Lin, Laser attenuation of the focused powder streams in coaxial laser cladding, *J. Laser Appl.* 12 (2000) 28, <http://dx.doi.org/10.2351/1.521910>.